ACS APPLIED MATERIALS & INTERFACES

Research Article

www.acsami.org

Ni and p-Cu_2O Nanocubes with a Small Size Distribution by Templated Electrodeposition and Their Characterization by Photocurrent Measurement

A. Wouter Maijenburg,[†,∥] Azusa N. Hattori,[‡] Moreno De Respinis,[§] Colleen M. McShane,[∥] Kyoung-Shin Choi,[∥,⊥] Bernard Dam,[§] Hidekazu Tanaka,[‡] and Johan E. ten Elshof*[,†]

[†]Inorganic Materials Science, MESA+ Institute for Nanotechnology, University of Twente, P.O. Box 217, 7500 AE Enschede, The Netherlands

[‡]Institute of Scientific and Industrial Research, Osaka University, 8-1 Mihogaoka, Ibaraki, Osaka 567-0047, Japan

[§]Materials for Energy Conversion and Storage Group, Delft University of Technology, Julianalaan 136, 2628 BL Delft, The Netherlands

[∥]Department of Chemistry, Purdue University, 560 Oval Drive, West Lafayette, Indiana 47907-2084, United States

ABSTRACT: A method for the reproducible formation of Ni and Cu_2O nanocubes with dimensions of 200−500 nm and a small size distribution is introduced. For this, the well-known templated electrodeposition technique was extended to cubic PMMA templates made by nanoimprint lithography. When making cubic templates in larger quantities, this method has the potential to become simple and cost-effective. This method was successfully used for the formation of Ni and p-Cu_2O nanocubes as well as for the formation of segmented nanobars containing both phases. The lateral dimensions of the nanocubes exactly resembled the dimensions of the template, and the height could be varied by adjusting the deposition time. Nanocubes formed via this method can remain attached to the substrate or can be dispersed in solution. p-Cu_2O is considered to be one of the most promising photocathode materials for solar water splitting. It is demonstrated that the activity of the p-Cu_2O nanocubes for photocatalytic water splitting can be measured, and it was found that the nanocube morphology enhances the photocatalytic activity compared to thin films.

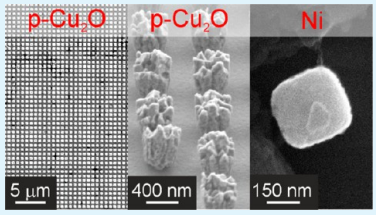

KEYWORDS: *electrochemical deposition, nickel, cuprous oxide, nanocubes, nanobars, multicomponent*

INTRODUCTION

The synthesis of nanoparticles of well-defined shape and size has attracted large interest over the past decades because the material properties and functionality can be tuned by changing the shape and size of the particles. In particular, the synthesis of nanocubes has attracted large interest. For self-assembly purposes, it is advantageous to have an object of cubic symmetry with well-defined facets. Park et al. showed that the assembly and disassembly of nanoparticles by DNA linkers strongly depends on the curvature of the exposed facets,[1] and other authors showed the high potential of nanocubes for self-assembly processes as well.[2−7] Nanocubes can also show catalytic performance. The catalytic activity depends on the crystal facet that is exposed and differs between polycrystalline and single-crystalline facets. For instance, Xu et al. investigated the electrocatalytic activity of Pt−Cu nanocubes for the oxidation of methanol and formic acid,[8,9] and Jalem et al. used Pt nanocube-mosaics for the electro-oxidation of methanol.[10] Nanocubes are also considered for other applications, for example, in photocatalysis,[11−14] fuel cells,[15,16] batteries,[17−19] biomedical applications,[20−23] and surface-enhanced Raman scattering.[24−29]

The most commonly used technique for making nanocubes in solution is the polyol process for Ag,[30−32] Cu_2O,[17,33] and α-$NaYF_4$ nanocubes.[34] Au nanocubes are typically prepared by electrochemical synthesis[35,36] or surfactant-mediated growth.[37−39] Other innovative techniques for nanocube synthesis include particle replication in nonwetting templates (PRINT),[40] biological synthesis,[41] and electrodeposition on graphene paper.[15] Unfortunately, none of these techniques allow for the synthesis of nanocubes of various materials having a small size distribution. Another disadvantage of these techniques is that the window of experimental conditions to make nanocubes is usually very small (i.e., a small deviation from the required conditions results in the formation of a heterogeneous distribution of nanoparticles with various sizes and shapes).

Templated electrodeposition is a widely used technique for the formation of nanowires and nanotubes of a desired composition that have a small size distribution.[42−45] The only requirement for templated electrodeposition is the availability of a template with the desired dimensions and shape and a conductive layer for electron transport. In the case of nanowires and nanotubes, track-etched polycarbonate (PCTE) and anodized aluminum oxide (AAO) membranes have typically been used as templates that are either commercially available or

Received: July 31, 2013
Accepted: October 1, 2013
Published: October 1, 2013

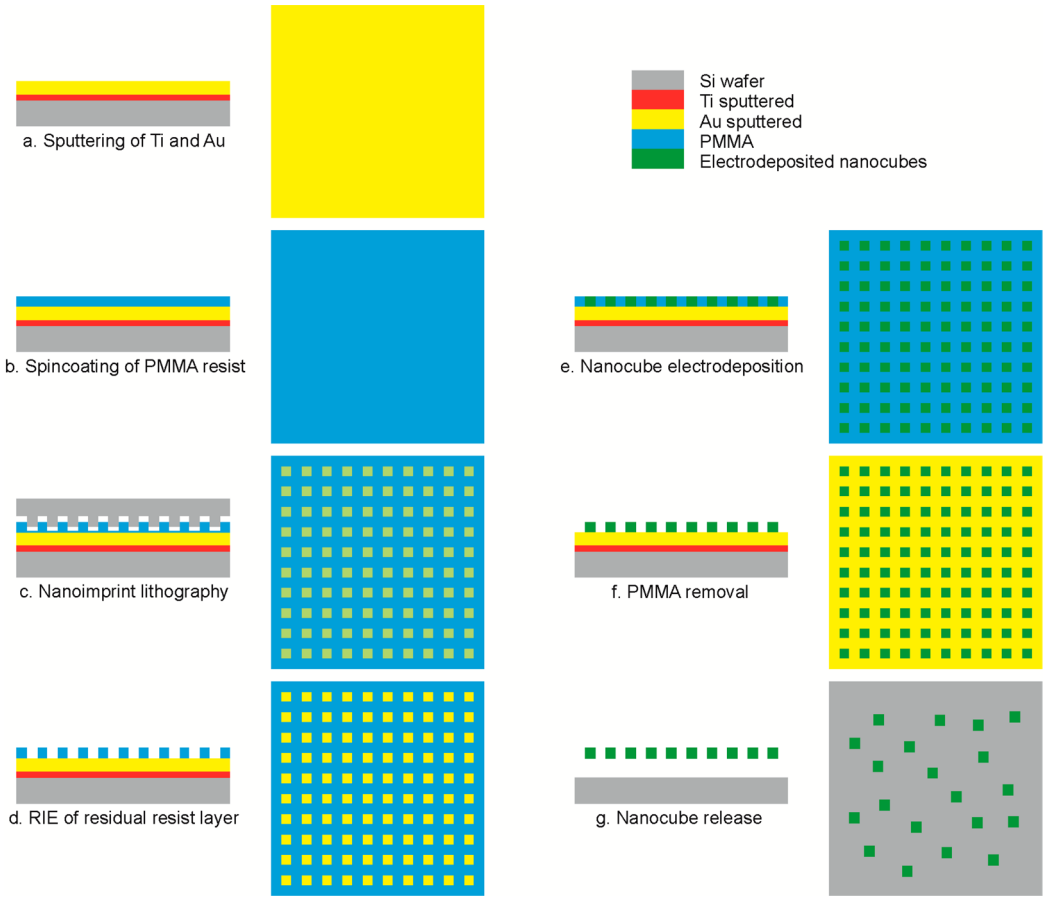

Figure 1. Schematic representation of template formation and nanocube electrodeposition: (a) Sputtering of Ti and Au on a clean Si wafer, (b) spincoating of PMMA, (c) nanoimprint lithography with the desired mask, (d) reactive-ion etching (RIE) of the residual resist layer, (e) electrodeposition of nanocubes inside the template, (f) removal of the PMMA template, and (g) release of nanocubes using Au etchant.

custom made. In both cases, billions of cylindrical pores are created within a few processing steps. Although templates containing cylindrical pores are readily available, templates containing cubic pores for templated electrodeposition of nanocubes have not been reported.

In this article, we present an approach to synthesize metal and metal-oxide nanocubes by templated electrodeposition in cubic templates formed by nanoimprint lithography (NIL). NIL is a promising technique to create templates with innovative shapes for templated electrodeposition because it can form patterns with a resolution as small as 10 nm over a large area with high throughput and low cost.[46−50] Once a mold is made (e.g., by e-beam lithography (EBL) or focused ion beam (FIB)), the mold can be reused as often as needed, and the NIL pattern will perfectly replicate the inverse of the mold. The most commonly used photoresist for NIL is polymethylmethacrylate (PMMA). Previously, Ross et al. used similar lithographically patterned resist layers containing cylindrical holes for the electrodeposition of magnetic nanostructures.[51,52]

The electrodeposition of Ni nanocubes is used as an example to show the feasibility of PMMA photoresist templates for templated electrodeposition of new types of nanostructures that can stay attached to the substrate or be dispersed in solution. We also deposited single-component p-Cu_2O nanocubes, which showed a higher photocatalytic activity towards H_2 evolution than p-Cu_2O films, and multicomponent nanobars of Ni and p-Cu_2O. It is envisaged that nanocubes and other nanostructures of desired composition as well as layered nanocubes containing multiple different materials can be made using this technique.

EXPERIMENTAL DETAILS

All chemicals used were purchased from commercial sources and used without further purification. Polymethylmethacrylate (PMMA) was purchased from Tokyo Ohka Kogyo Co., LTD. Nickel sulfate hexahydrate ($NiSO_4·6H_2O$, purity 99%), boric acid (H_3BO_3, purity 99.99%), and dichloromethane (CH_2Cl_2, purity 99.9%) were purchased from Merck. Copper sulfate pentahydrate ($CuSO_4·5H_2O$, p.a. quality) and sodium sulphate (Na_2SO_4, p.a. quality) were purchased from Boom Chemie. Lactic acid (extra pure), sodium hydroxide (NaOH, purity 98.5%), sulfuric acid (H_2SO_4, 96% in water), and dipotassium phosphate trihydrate ($K_2HPO_4·3H_2O$, purity 99+%) were purchased from Acros Organics. Tetrahydrofuran (THF, purity 99%) and gold etchant were purchased from Sigma-Aldrich. Acetone was purchased from Assink Chemie. Milli-Q water with a resistivity of 18.2 MΩ cm was used in all experiments.

The technique for making nanopatterns is reported elsewhere,[49] with the only difference in the technique used in the present study being that Au-coated Si wafers were used as substrate for templated electrodeposition. Essentially, 4 in. Si(100) wafers were coated with a ∼15 nm Ti and ∼75 nm Au layer using a PerkinElmer sputtering machine operating at 50 W at a deposition pressure of 2×10^{-2} mbar and Ar as sputtering gas. After spincoating a layer of PMMA on top of these substrates, various quartz molds containing cubic pillar patterns with a height of 200 nm (NTT-AT Nanofabrication Co., Japan) were used for UV−NIL at room temperature using a force of 600 N for 2 min of UV exposure by a nanoimprinter (Eitre 3, Obducat). The

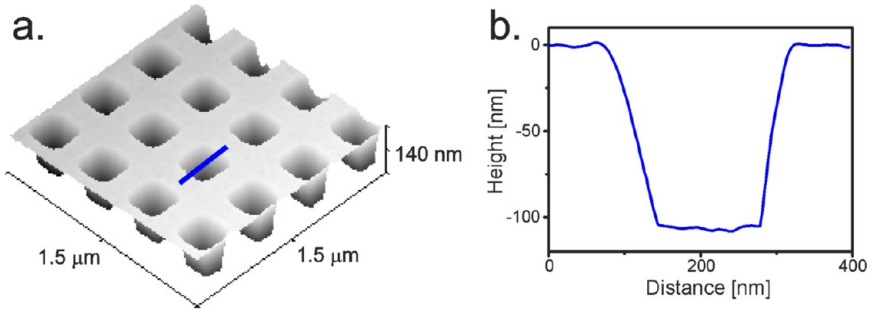

Figure 2. (a) AFM topography image and (b) height profile of a cubic PMMA template formed by UV−NIL.

residual layers were removed by a CF_4 and O_2 plasma process using a reactive-ion etching system (RIE-10NR, Samco, Japan).

Templated electrodeposition was carried out by connecting the Au substrate containing the patterns to the working electrode in a conventional three-electrode setup using a Pt sheet (Metrohm Autolab) as the counter electrode and Ag/AgCl in 3 M KCl (Metrohm Autolab) as the reference electrode. All reported potentials are given with respect to the reference electrode unless otherwise stated. The electrodes were connected to an Autolab PGSTAT 128N potentiostat. Ni was deposited at −1.00 V from an aqueous electrolyte solution containing 0.23 M $NiSO_4{\cdot}6H_2O$ and 0.15 M H_3BO_3. p-Cu_2O was deposited at −0.4 V from an aqueous electrolyte containing 0.02 M $CuSO_4$ and 0.4 M lactic acid. Before deposition, the solution was adjusted to pH 11 using NaOH and H_2SO_4 and heated to a temperature of 60 °C. During deposition, the current was monitored as a function of time using NOVA 1.9 software (Metrohm Autolab).

After deposition, the PMMA patterns were dissolved by immersing the substrates in either acetone or THF. The Au layer could be removed by immersing the substrates in a commercial gold etchant containing KI/I_2. For SEM imaging of the dispersed nanocubes, the gold etchant solution was first replaced at least five times with water by centrifugation at 10 000 rpm for 15 min using a Hermle Z36HK centrifuge. Subsequently, water was replaced with acetone by centrifugation for three times. The complete process of template formation and nanocube electrodeposition is schematically shown in Figure 1.

Tapping-mode atomic force microscopy (AFM) images were taken using a Veeco Dimension Icon. SEM images were taken using a Zeiss HR-LEO 1550 FEG (field-emission gun) SEM and a Zeiss Merlin HRSEM. X-ray diffraction (XRD) on the nanocubes was performed with a Bruker D2 Phaser with a Cu Kα X-ray source at a wavelength of 1.54 Å.

Photoelectrochemical characterization was carried out in an aqueous solution containing 1 M Na_2SO_4 and 0.1 M K_2HPO_4, which was adjusted to pH 4.9 using H_2SO_4 and NaOH. The solution was purged with nitrogen prior to and during the measurements to remove any dissolved oxygen. Potential control was provided by an EG&G PAR 283 potentiostat in a three-electrode cell with a fused silica window. An XR300 radiometer analytical Ag/AgCl electrode and a coiled Pt wire were used as reference and counter electrodes, respectively. White-light photocurrent densities were measured under simulated AM1.5 solar illumination (100 mW/cm^2) with a Newport Sol3A Class AAA solar simulator (type 94023A-SR3). For the nanocube samples, the measured current was multiplied by 2.5 as correction factor so that only the top surface area of the nanocubes was taken into account, which was 40% of the total surface area. The potential of the photocurrent measurements was converted to the NHE reference electrode by

$$E\ (\text{vs NHE}) = E\ (\text{vs Ag/AgCl}) + E_{\text{Ag/AgCl}}(\text{ref}) + 0.0591\ \text{V} \times \text{pH} \quad (1)$$

$$E_{\text{Ag/AgCl}}(\text{ref}) = 0.1976\ \text{V vs NHE at } 25°\text{C} \quad (2)$$

RESULTS AND DISCUSSION

Figure 2 shows an AFM image of one of the cubic templates that was used for the experiments shown in Figure 3. The cubic hole patterns in this template have lateral dimensions of 200 × 200 nm^2 and a depth of 100 nm. For the results shown in Figures 4 and 6, templates with a depth of at least 300 nm were used. The major drawback of all lithography techniques for the formation of templates for nanocubes is that it is currently impossible to create perfectly sharp edges. However, for the proposed applications in self-assembly and photocurrent measurements, this does not significantly influence the performance.

Ni was electrodeposited inside these cubic templates following a recipe that resulted in well-controlled growth and smooth films. Ni electrodeposition was carried out for 40−105 s in templates like the one presented in Figure 2. A chronoamperogram (I−t curve) was recorded during deposition to monitor the deposition rate of Ni in these templates (Figure 3a,b). As indicated by the arrow in Figure 3a, the current slightly increased after 50 s of deposition, indicating a gradually increasing growth rate because of "mushrooming" on top of the template.[45] After 70 s, the deposition rate became constant as the mushrooming stage was completed, and a relatively flat surface covering the whole sample was formed. Because the deposition consisted of two consecutive electrodeposition steps, the I−t curve shows the charging of the electrical double layer around 45 s when the second deposition step of 60 s initiated. The mushrooming effect was also observed by AFM and SEM (Figure 3c,e,g,i). However, when deposition was terminated before the Ni phase reached the top of the template, as indicated by the absence of a change in current in Figure 3b, a relatively flat nanocube top surface was observed (Figure 3d,f,h,j). The roughness of the top surface of these nanocubes was estimated with the root mean square (rms) method and was found to be 5 ± 1 nm, which is in the same range as the rms value of a Ni film made by electrodeposition (~6 nm). From the observations that mushrooming started after 50 s in a template with a depth of 100 nm, that a mushroom with a 20 nm thick top was deposited after 60 s, and that deposition was terminated 20 nm underneath the template surface after 40 s of deposition, a growth rate for Ni nanocubes of ~2 nm/s can be derived.

After the PMMA resist was dissolved in acetone, stable mushrooms or nanocubes remained on the Au substrate (Figure 3g,h). Templated electrodeposition perfectly replicates the shape of the pattern including the rounded edges of the template, as seen in the formed nanocubes (Figure 3h). The open spaces in these figures represent hole patterns where no deposition took place, probably because of the presence of a

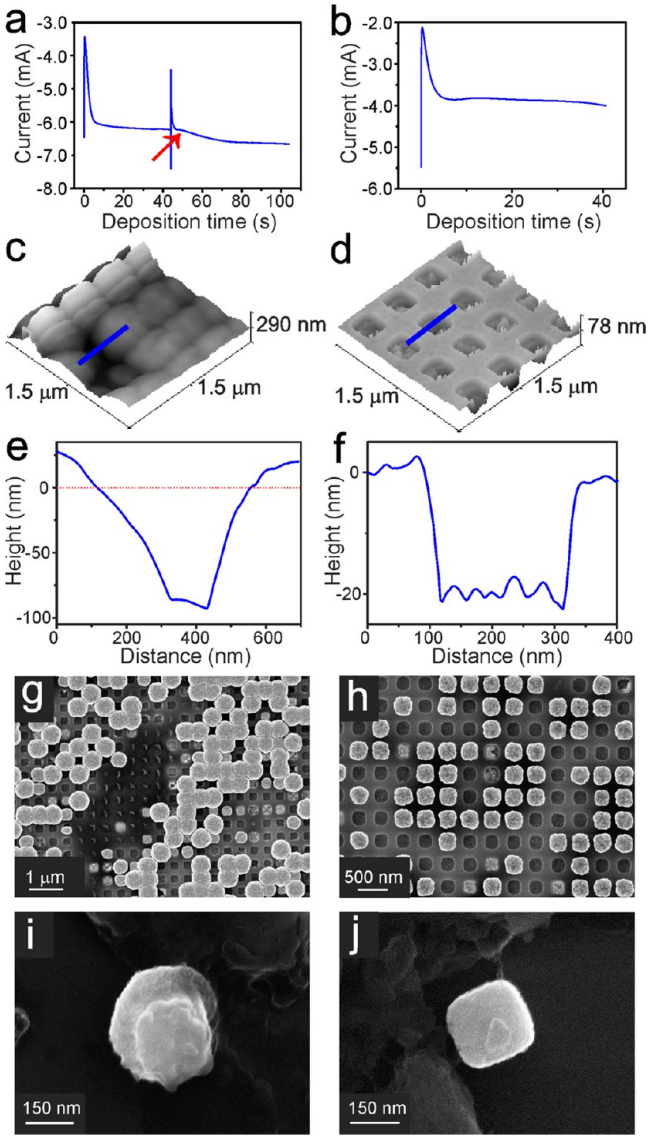

Figure 3. Ni electrodeposited inside PMMA templates with squared holes on Au. (a) Chronoamperogram of 105 s deposition, (b) chronoamperogram of 40 s deposition, (c) AFM topography image of nanocubes inside the template after 60 s deposition, (d) AFM topography image of nanocubes inside the template after 40 s deposition, (e) AFM height profile taken at the blue line in panel c where the dotted red line indicates the location of the top surface of the pattern, (f) AFM height profile taken at the blue line in panel d, (g) SEM image of nanocubes deposited for 60 s after dissolving the PMMA template, (h) SEM image of nanocubes deposited for 40 s after dissolving the PMMA template, (i) SEM image of nanocubes deposited for 60 s after dissolving the Au substrate, and (j) SEM image of nanocubes deposited for 40 s after dissolving the Au substrate.

small residual resist layer that electrically shielded the conductive Au substrate from the liquid phase by preventing electron transfer. When the residual resist layer was completely removed by a plasma etching process before electrodeposition, all holes were filled as illustrated in Figure 4. Figure 3i,j illustrates the possibility of dispersing the deposited nanocubes in a solvent and drop casting them onto another substrate. For this, the Au substrate was dissolved in Au etchant to release the nanocubes from the substrate. After subsequent centrifugation, the Au etchant solution was first replaced by distilled water and then by acetone for fast drying and SEM imaging. As can be seen from the SEM images in Figure 3i,j, the process to dissolve the Au substrate and immerse the Ni nanocubes did not damage the dispersed nanocubes. It is noted that this specific Au etchant is compatible with Ni, so care should be taken when dispersing nanocubes of a different composition.

Metal oxides were also deposited in these cubic templates. Figure 4a–e shows p-type doped Cu_2O nanocubes of different sizes. It is interesting to note that for these nanocubes their surface is rougher than that of the Ni nanocubes because each Cu_2O cube is composed of multiple very small crystallites. When the same p-Cu_2O electrodeposition process was carried out on an ITO or Au substrate without the use of a template, the formation of larger crystallites with a lateral dimension of ~1 μm or more and cubic morphology was observed.[53,54] The p-Cu_2O nanocubes deposited in the nano-sized cubic templates are composed of smaller crystallites, which suggests that the nucleation of Cu_2O in the nano-sized template takes place more easily than without template. The deposition of Cu_2O is a two-step process in which Cu^+ ions are formed by electrochemical reduction of Cu^{2+}, and Cu^+ ions are subsequently precipitated to form Cu_2O because of the limited solubility of Cu^+ in water. Therefore, the nucleation of Cu_2O requires the build up of Cu^+ ions exceeding its solubility limit ($\log[Cu^+] = -0.84 - pH$).[55] When Cu^+ ions are generated within the nanopores of a template, diffusion of Cu^+ ions away from the electrode should be much more difficult compared to the diffusion of Cu^+ ions along the planar electrode surface at which they were generated. As a result, severe supersaturation of Cu^+ ions can be easily achieved in the nanopores, facilitating the nucleation process. The formation of multiple smaller crystallites compared to the formation of fewer larger crystals is a good indication that the nucleation process is more favored than the growth process.

When we compare the nucleation densities of p-Cu_2O within the different dimensions of the nanocube templates used, we observed the largest nucleation density for the templates with lateral dimensions of 400 and 500 nm depth followed by the templates with lateral dimensions of 200 and 350 nm depth and then the templates with lateral dimensions of 500 and 600 nm depth. This indicates that with the current samples no correlation between nucleation density and lateral and vertical dimensions was found. Detailed inspection of the SEM images of the nanocubes grown within the smaller (200 nm) templates showed the intergrowth of only one to three crystallites within a single pore (Figure 4a). Because of the preferred growth direction of these crystallites, they were only attached to the substrate by a few nucleation points and therefore had poor adhesion to the substrate and easily washed off during template removal. This can be seen in the top left part of Figure 4a where the PMMA has been dissolved and the crystals inadvertently washed away. The bottom right part of this figure shows that the crystals that are still surrounded by undissolved PMMA are still present. Using a template with lateral dimensions of 400 (Figure 4c–e) or 500 nm (Figure 4b) resulted in the intergrowth of more crystallites within one hole, which enhanced the stability of the respective nanocubes. A closer look at the tilted SEM image in Figure 4e shows that these nanocubes display pillar-like growth with a diameter of ~50–100 nm and roughly shaped sides and top surfaces.

Cu_2O is an interesting material for applications in solar cells and as a photocathode in photoelectrochemical water splitting because it is a cheap and abundant material with a direct band gap of 2.0 eV. With the p-Cu_2O nanocubes still attached to the

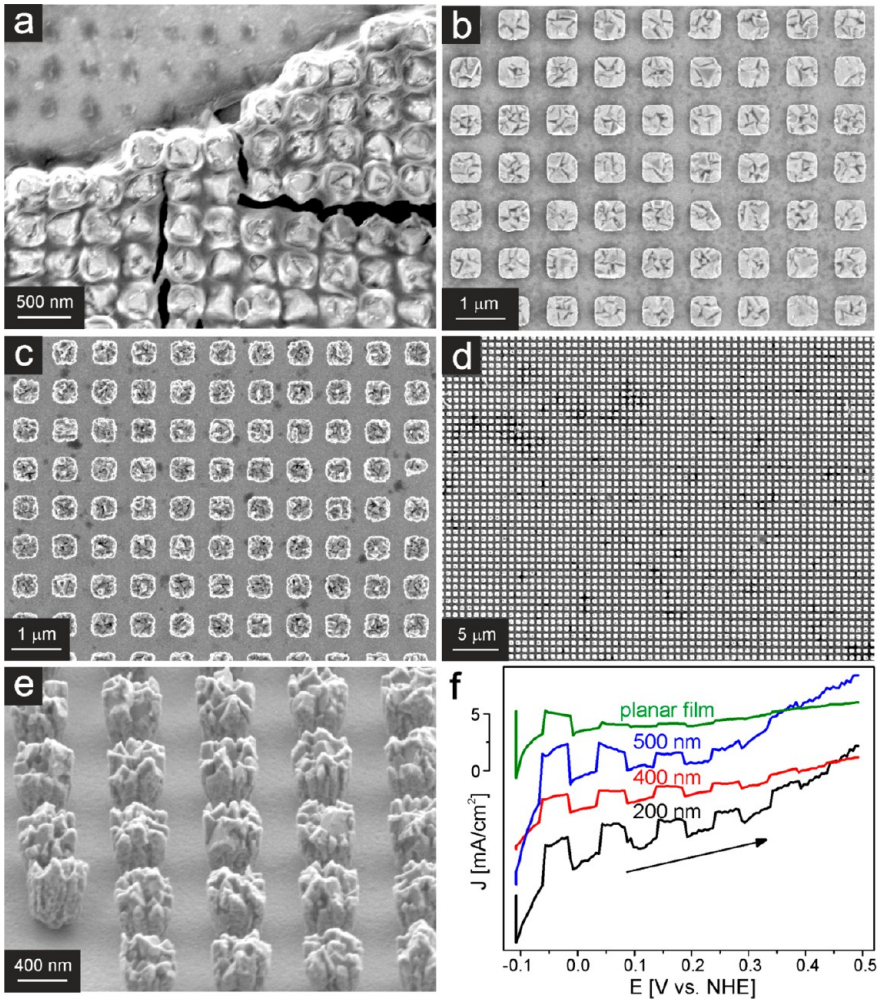

Figure 4. (a–d) Top-view SEM images of p-Cu_2O nanocubes made by templated electrodeposition for 4 min in a cubic template with dimensions of (a) 200 nm lateral and 350 nm depth, (b) 500 nm lateral and 600 nm depth, (c, d) 400 nm lateral and 500 nm depth, and (e) 45° tilted SEM image of p-Cu_2O nanocubes with lateral dimensions of 400 and 500 nm depth after template removal. (f) Photocurrent LSV curves of p-Cu_2O nanocubes and p-Cu_2O films in 1 M Na_2SO_4 and 0.1 M K_2HPO_4 at pH 4.9 continuously bubbled with N_2; the scan rate was 10 mV/s in the positive direction and the light was chopped with intervals of 5 s. For the sake of comparison, the electrolyte used by Grätzel and co-workers[56] was employed in this study. For the sake of clarity, the LSV curves were offset.

substrate after PMMA removal, the photocurrent was measured, and the results are shown in Figure 4f for p-Cu_2O nanocube samples with different lateral dimensions. The photocurrent of a planar p-Cu_2O film is also shown for comparison. All samples were electrodeposited for 4 min from the previously mentioned p-Cu_2O plating solution. A few differences in efficiency between the nanocubes and the film are apparent from this graph: the nanocubes show (i) a higher photocurrent at 0 V versus NHE, (ii) noticeable photocurrent at more positive potentials (e.g., higher than 0.3 V vs NHE), and (iii) a higher dark current. (i) The higher photocurrent (up to ~3 mA/cm^2 at 0 V vs NHE for the nanocube samples vs ~1.5 mA/cm^2 for the films) may be explained by the larger true surface area of a nanostructure. It is noteworthy that the photocurrent of the nanocubes was slightly higher than the bare p-Cu_2O films measured by Grätzel and co-workers in the same electrolyte,[56] whereas the photocurrent of our films was slightly lower. To the best of our knowledge, the only difference between the two measurements was that we did not use Pt nanoparticles, which is a well-known catalyst for H_2 formation and thereby increased the photostability of p-Cu_2O. However, the increase in photocurrent achieved by the nanocube electrodes was not as high as the ca. five-fold increase achieved in surface area by nanocube formation over the planar film electrode. This suggests that the nanocube formation may also have caused an adverse effect such as an increase in surface states that would result in decreased photocurrent. (ii) In addition to the explanation in (i) for the higher photocurrent at 0 V versus NHE, the noticeable photocurrent at more positive potentials for the nanocube samples compared to a negligible photocurrent for the planar film electrode may be due to an earlier photocurrent onset potential at more positive potentials and/or an enhanced photostability of the nanocubes. The first explanation, an earlier photocurrent onset potential, often results when the nanostructure is incorporated into the photoelectrode because the presence of a nanostructure generally helps electron-hole separation by increasing the relative volume of the depletion layer and/or reducing the distance that the minority carriers need to travel to reach the electrode/electrolyte interface.[57,58] Because Cu_2O is known to photodegrade easily during photocurrent measurements,[56] the linear sweep voltammetry (LSV) curves in Figure 4f were measured in the positive direction so that the photodegradation effect on the photocurrent measured at 0 V versus NHE was

minimized. Figure 5 shows LSV curves of two different films in which the scan direction were opposite. Regardless of the scan

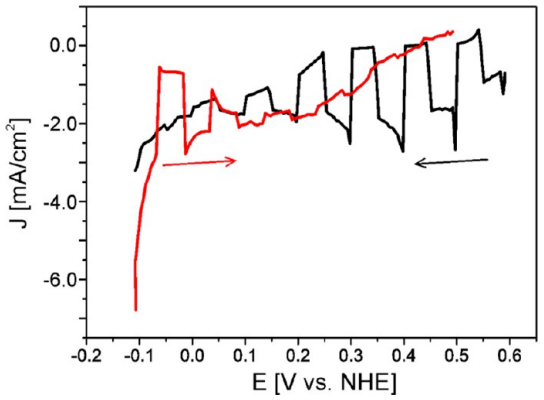

Figure 5. Photocurrent LSV curves of two different p-Cu_2O films in 1 M Na_2SO_4 and 0.1 M K_2HPO_4 at pH 4.9 continuously bubbled with N_2. The scan rate was 10 mV/s in the negative direction (black curve) or in the positive direction (red curve), and the light was chopped with intervals of 5 s.

direction, for both samples the photocurrent decreased as the measurement continued. Therefore, these LSV curves show the dependence of the current density not only on the potential but also on the degradation with time. For this reason, the second explanation for the increased photocurrent at more positive potentials could be an increased photostability of the nanocubes. The photostability of p-Cu_2O for photoelectrochemical water reduction can be further increased by passivation with a coating of Al-doped ZnO and TiO_2, as demonstrated by Grätzel and co-workers.[56] However, further investigation into the origin of the enhanced photocurrent observed in this study is necessary, which is outside the scope of this study. (iii) The higher cathodic dark current observed for the nanocube electrodes was represented by the deviation from perfectly horizontal dark current lines for the 200 and 500 nm nanocube electrodes especially. This can be explained by a secondary reaction taking place in which the photodegradation product, CuO, was reduced back to Cu_2O, which again could be explained by the larger true surface area of the nanocube samples.

The same technique was also applied to form nanocubes with both Ni and p-Cu_2O segments within the same template, yielding segmented nanocubes composed of both phases. It is noted that the combination of Ni and p-Cu_2O is merely a model system for which no clear application yet exists, but it is one that illustrates the possibility to form nanocubes consisting of two or more different phases, which is unique for this technique. Figure 6 shows examples of nanobars composed of Ni at the bottom and p-Cu_2O at the top. It is interesting to note that the p-Cu_2O grown inside this type of templates when Ni was deposited first appear much smoother. A closer look at the top of these nanocubes, where the top of the template used to be and where mushrooming was expected for templated electrodeposition of polycrystalline materials, reveals that the p-Cu_2O phase grew as a large crystal on top of the Ni phase. Apparently, the Ni phase acted as a perfect seed layer for the growth of large p-Cu_2O crystals. The porous appearance of the p-Cu_2O phase, which is also visible in these SEM images, is probably induced by etching during template removal. Although harsh cleaning conditions were used to ensure the dissolution of all PMMA before SEM imaging, ~50% of the nanobars still appeared intact and contained both Ni and Cu_2O. These harsh conditions included immersion in acetone and THF for several days and ultrasonication in these solvents for several hours. The EDX spectra in Figure 6d,e confirmed the deposition of both a Ni and a Cu containing phase within the

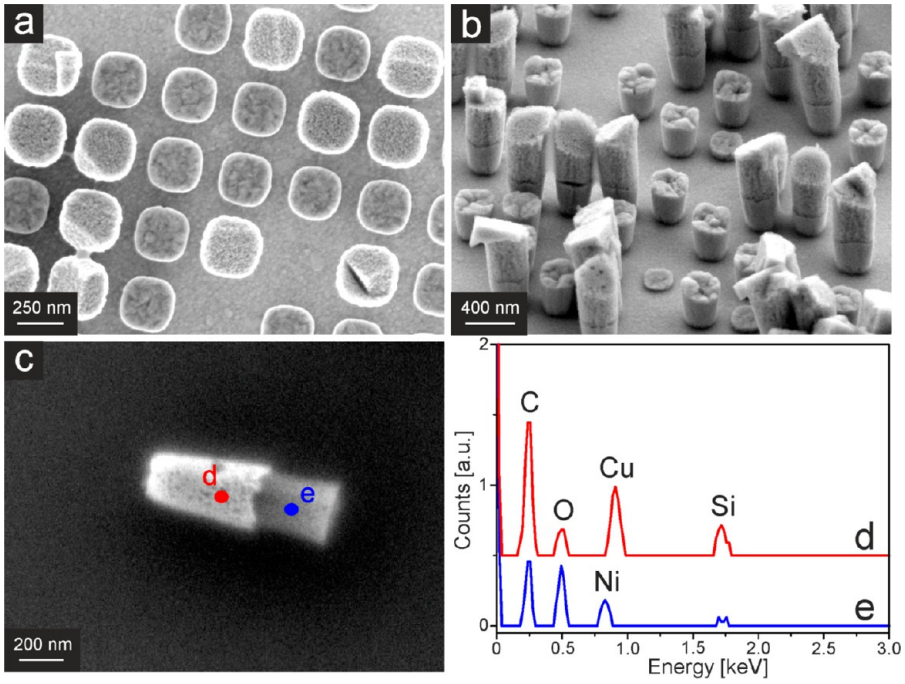

Figure 6. (a) Top-view and (b) 45° tilted SEM images of bifunctional Ni|p-Cu_2O nanobars made by sequential templated electrodeposition in a cubic template with dimensions of 200 × 200 nm^2 after template removal, (c) SEM image after release from the substrate of the same nanobars, and EDX spectra of (d) the p-Cu_2O segment and (e) the Ni segment of the horizontally placed nanobar in panel c.

nanobar of Figure 6c. The Si peaks in Figure 6d,e originate from the Si substrate, and both C peaks and the O peak in Figure 6e originate from undissolved organic template residues.

The phases of the nanocubes made in this study were investigated with X-ray diffraction (XRD). As shown in Figure 7, the main phases of the respective nanocubes are Ni and

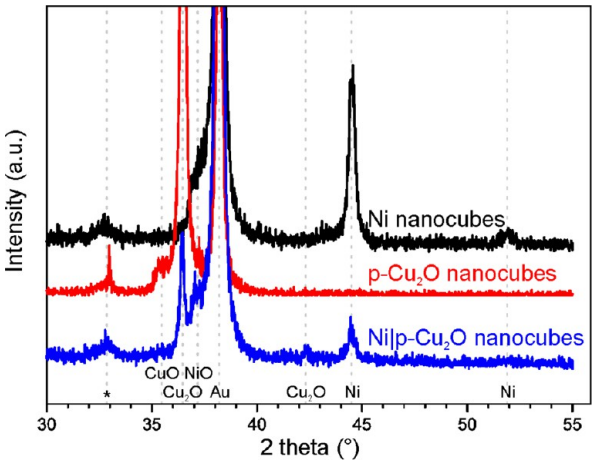

Figure 7. XRD patterns of Ni nanocubes (black line), p-Cu_2O nanocubes (red line), and segmented Ni|p-Cu_2O nanocubes with lateral dimensions of 200 nm. Diffraction peaks were assigned to Au (PDF no. 00-004-0784), Ni (PDF no. 00-004-0850), Cu_2O (PDF no. 00-005-0667), NiO (PDF no. 00-047-1049), and CuO (PDF no. 00-048-1548). An unknown impurity phase is denoted with an asterisk (*).

Cu_2O. It is likely that the minor peaks for CuO and NiO originate from oxidized surface layers and are not formed during deposition. The observed Au peaks originate from the substrate used for nanocube growth. An unidentified impurity phase, denoted with an asterisk, probably originates from the substrate because it is present in all samples, but the reference patterns for Si, SiO_2, Ti, and Au did not overlap.

The ability of this method to yield nanocubes on a substrate as well as the possibility of detaching them from the substrate opens up prospects for their use in many different types of applications. However, it should be noted that although this method worked perfectly for the formation of Ni and p-Cu_2O nanocubes more effort is needed to realize the formation of nanocubes of other compositions. These efforts include the optimization of the electrodeposition conditions, for example, the pH of the electrolyte and pulsed electrodeposition. It is expected that with these improvements nanocubes can also be made from many more materials via the same procedure. With the possibility of making multicomponent nanocubes within the same template, it is also possible to make different types of functional segmented nanocubes, as demonstrated here for the case of Ni|p-Cu_2O.

CONCLUSIONS

A new type of template was introduced that extends the method of templated electrodeposition to the formation of nanocubes, as was demonstrated by the formation of Ni and p-Cu_2O nanocubes and segmented nanobars containing both phases. The lateral dimensions of the formed nanocubes can be controlled by the pattern on the master used for NIL, and the height can be controlled by the deposition time. After deposition, the nanocubes can either remain attached to the substrate or can be removed from the substrate by dissolving the Au layer. The Ni nanocubes were very smooth, and the rms roughness value of the top layer was found to be comparable to the rms value of Ni films made by electrodeposition without template. The roughness of p-Cu_2O nanocubes was much higher because a high concentration of small crystallites were nucleated within the templates. Photocurrent measurements of p-Cu_2O nanocubes were compared to photocurrent measurements of p-Cu_2O films, and it was shown that the nanocubes show a higher photocurrent at 0 V versus NHE, an increased photocurrent at more positive potentials (e.g., 0.3 V vs NHE), and a higher dark current. These observed differences can be explained by the higher surface area of the nanocube electrodes and an earlier photocurrent onset potential and/or increased photostability of the nanocubes.

AUTHOR INFORMATION

Corresponding Author

*E-mail: j.e.tenelshof@utwente.nl. Tel: +31 (0)53 489 2695.

Present Address

[⊥]University of Wisconsin−Madison, 1101 University Avenue, Madison, Wisconsin 53706, United States.

Notes

The authors declare no competing financial interest.

ACKNOWLEDGMENTS

Financial support from the Chemical Sciences division of the Netherlands Organization for Scientific Research (NWO-CW) in the framework of the TOP program as well as from the Fulbright Center in The Netherlands is gratefully acknowledged. Financial support to K.S.C. and C.M.M. from the Division of Chemical Sciences, Geosciences, and Biosciences, Office of Basic Energy Sciences of the U.S. Department of Energy through grant DE-FG02-05ER15752 is also gratefully acknowledged.

REFERENCES

(1) Park, H. G.; Joo, J. H.; Kim, H. G.; Lee, J. S. *J. Phys. Chem. C* **2012**, *116*, 2278−2284.
(2) Gao, B.; Arya, G.; Tao, A. R. *Nat. Nanotechnol.* **2012**, *7*, 433−437.
(3) Mimura, K. I.; Dang, F.; Kato, K.; Imai, H.; Wada, S.; Haneda, H.; Kuwabara, M. *Jpn. J. Appl. Phys.* **2011**, 50.
(4) Rabin, O. *Nat. Nanotechnol.* **2012**, *7*, 419−420.
(5) Chen, H.; Sun, Z.; Ni, W.; Woo, K. C.; Lin, H. Q.; Sun, L.; Yan, C.; Wang, J. *Small* **2009**, *5*, 2111−2119.
(6) Mahmoud, M. A.; El-Sayed, M. A. *J. Phys. Chem. C* **2008**, *112*, 14618−14625.
(7) Meijer, J. M.; Hagemans, F.; Rossi, L.; Byelov, D. V.; Castillo, S. I. R.; Snigirev, A.; Snigireva, I.; Philipse, A. P.; Petukhov, A. V. *Langmuir* **2012**, *28*, 7631−7638.
(8) Xu, D.; Liu, Z.; Yang, H.; Liu, Q.; Zhang, J.; Fang, J.; Zou, S.; Sun, K. *Angew. Chem.* **2009**, *121*, 4281−4285.
(9) Xu, D.; Bliznakov, S.; Liu, Z.; Fang, J.; Dimitrov, N. *Angew. Chem., Int. Ed.* **2010**, *49*, 1282−1285.
(10) Jalem, R.; Koike, R.; Yang, Y.; Nakayama, M.; Nogami, M. *Nano Res.* **2011**, *4*, 746−758.
(11) In, S. I.; Vaughn Ii, D. D.; Schaak, R. E. *Angew. Chem., Int. Ed.* **2012**, *51*, 3915−3918.
(12) Chen, D.; Yoo, S. H.; Huang, Q.; Ali, G.; Cho, S. O. *Chem.—Eur. J.* **2012**, *18*, 5192−5200.
(13) Tang, J.; Cheng, G.; Zhou, H.; Yang, H.; Lu, Z.; Chen, R. *J. Nanosci. Nanotechnol.* **2012**, *12*, 4028−4034.
(14) Zheng, Z.; Huang, B.; Qin, X.; Zhang, X.; Dai, Y. *J. Colloid Interface Sci.* **2011**, *358*, 68−72.

(15) Gao, H.; Wang, Y.; Xiao, F.; Ching, C. B.; Duan, H. *J. Phys. Chem. C* **2012**, *116*, 7719−7725.
(16) Wu, H.; Chen, W. *J. Am. Chem. Soc.* **2011**, *133*, 15236−15239.
(17) Park, J. C.; Kim, J.; Kwon, H.; Song, H. *Adv. Mater.* **2009**, *21*, 803−807.
(18) Chen, L.; Shen, L.; Nie, P.; Zhang, X.; Li, H. *Electrochim. Acta* **2012**, *62*, 408−415.
(19) Liu, R.; Yang, S.; Wang, F.; Lu, X.; Yang, Z.; Ding, B. *ACS Appl. Mater. Interfaces* **2012**, *4*, 1537−1542.
(20) Tokonami, S.; Yamamoto, Y.; Shiigi, H.; Nagaoka, T. *Anal. Chim. Acta* **2012**, *716*, 76−91.
(21) Chen, J.; Wiley, B.; Li, Z. Y.; Campbell, D.; Saeki, F.; Cang, H.; Au, L.; Lee, J.; Li, X.; Xia, Y. *Adv. Mater.* **2005**, *17*, 2255−2261.
(22) Guardia, P.; Di Corato, R.; Lartigue, L.; Wilhelm, C.; Espinosa, A.; Garcia-Hernandez, M.; Gazeau, F.; Manna, L.; Pellegrino, T. *ACS Nano* **2012**, *6*, 3080−3091.
(23) Skrabalak, S. E.; Chen, J.; Au, L.; Lu, X.; Li, X.; Xia, Y. *Adv. Mater.* **2007**, *19*, 3177−3184.
(24) Sisco, P. N.; Murphy, C. J. *J. Phys. Chem. A* **2009**, *113*, 3973−3978.
(25) Camargo, P. H. C.; Au, L.; Rycenga, M.; Li, W.; Xia, Y. *Chem. Phys. Lett.* **2010**, *484*, 304−308.
(26) Camargo, P. H. C.; Rycenga, M.; Au, L.; Xia, Y. *Angew. Chem., Int. Ed.* **2009**, *48*, 2180−2184.
(27) McLellan, J. M.; Siekkinen, A.; Chen, J.; Xia, Y. *Chem. Phys. Lett.* **2006**, *427*, 122−126.
(28) Rycenga, M.; Kim, M. H.; Camargo, P. H. C.; Cobley, C.; Li, Z. Y.; Xia, Y. *J. Phys. Chem. A* **2009**, *113*, 3932−3939.
(29) Santos Costa, J. C.; Ando, R. A.; Sant'ana, A. C.; Rossi, L. M.; Santos, P. S.; Temperini, M. L. A.; Corio, P. *Phys. Chem. Chem. Phys.* **2009**, *11*, 7491−7498.
(30) Darmanin, T.; Nativo, P.; Gilliland, D.; Ceccone, G.; Pascual, C.; De Berardis, B.; Guittard, F.; Rossi, F. *Colloids Surf., A* **2012**, *395*, 145−151.
(31) Sun, Y.; Xia, Y. *Proc. SPIE* **2003**, *5224*, 43−52.
(32) Zhu, J.; Kan, C.; Zhu, X.; Wan, J. G.; Han, M.; Zhao, Y.; Wang, B.; Wang, G. *J. Mater. Res.* **2007**, *22*, 1479−1485.
(33) Huang, L.; Peng, F.; Yu, H.; Wang, H. *Mater. Res. Bull.* **2008**, *43*, 3047−3053.
(34) Qin, R.; Song, H.; Pan, G.; Zhao, H.; Ren, X.; Liu, L.; Bai, X.; Dai, Q.; Qu, X. *J. Cryst. Growth* **2009**, *311*, 1559−1564.
(35) Huang, C. J.; Chiu, P. H.; Wang, Y. H.; Chen, W. R.; Meen, T. H. *J. Electrochem. Soc.* **2006**, *153*, D129−D133.
(36) Huang, C. J.; Wang, Y. H.; Chiu, P. H.; Shih, M. C.; Meen, T. H. *Mater. Lett.* **2006**, *60*, 1896−1900.
(37) Kou, X.; Sun, Z.; Yang, Z.; Chen, H.; Wang, J. *Langmuir* **2009**, *25*, 1692−1698.
(38) Kundu, S.; Panigrahi, S.; Praharaj, S.; Basu, S.; Ghosh, S. K.; Pal, A.; Pal, T. *Nanotechnology* **2007**, *18*, 075712.
(39) Sau, T. K.; Murphy, C. J. *J. Am. Chem. Soc.* **2004**, *126*, 8648−8649.
(40) Merkel, T. J.; Herlihy, K. P.; Nunes, J.; Orgel, R. M.; Rolland, J. P.; Desimone, J. M. *Langmuir* **2010**, *26*, 13086−13096.
(41) Kalishwaralal, K.; Deepak, V.; Ram Kumar Pandian, S.; Gurunathan, S. *Bioresour. Technol.* **2009**, *100*, 5356−5358.
(42) Aranda, P.; García, J. M. *J. Magn. Magn. Mater.* **2002**, *249*, 214−219.
(43) Maas, M. G.; Rodijk, E. J. B.; Maijenburg, W.; ten Elshof, J. E.; Blank, D. H. A. *Mater. Res. Soc. Symp. Proc.* **2010**, *1206*, 1−6.
(44) She, G.; Mu, L.; Shi, W. *Recent Pat. Nanotechnol.* **2009**, *3*, 182−191.
(45) Toimil Molares, M. E.; Buschmann, V.; Dobrev, D.; Neumann, R.; Scholz, R.; Schuchert, I. U.; Vetter, J. *Adv. Mater.* **2001**, *13*, 62−65.
(46) Chou, S. Y.; Krauss, P. R.; Zhang, W.; Guo, L.; Zhuang, L. *J. Vac. Sci. Technol., B: Microelectron. Nanometer Struct.* **1997**, *15*, 2897−2904.
(47) Austin, M. D.; Ge, H.; Wu, W.; Li, M.; Yu, Z.; Wasserman, D.; Lyon, S. A.; Chou, S. Y. *Appl. Phys. Lett.* **2004**, *84*, 5299−5301.
(48) Cha, N. G.; Kanki, T.; Tanaka, H. *Nanotechnology* **2011**, *22*, 185306.
(49) Cha, N. G.; Lee, B. K.; Kanki, T.; Lee, H. Y.; Kawai, T.; Tanaka, H. *Nanotechnology* **2009**, *20*, 395301.
(50) Hattori, A. N.; Ono, A.; Tanaka, H. *Nanotechnology* **2011**, *22*, 415301.
(51) Ross, C. A.; Haratani, S.; Castaño, F. J.; Hao, Y.; Hwang, M.; Shima, M.; Cheng, J. Y.; Vögeli, B.; Farhoud, M.; Walsh, M.; Smith, H. I. *J. Appl. Phys.* **2002**, *91*, 6848−6853.
(52) Ross, C. A.; Smith, H. I.; Savas, T.; Schattenburg, M.; Farhoud, M.; Hwang, M.; Walsh, M.; Abraham, M. C.; Ram, R. J. *J. Vac. Sci. Technol., B: Microelectron. Nanometer Struct.* **1999**, *17*, 3168−3176.
(53) McShane, C. M.; Choi, K. S. *Phys. Chem. Chem. Phys.* **2012**, *14*, 6112−6118.
(54) McShane, C. M.; Siripala, W. P.; Choi, K. S. *J. Phys. Chem. Lett.* **2010**, *1*, 2666−2670.
(55) Jang, H. S.; Kim, S. J.; Choi, K. S. *Small* **2010**, *6*, 2183−2190.
(56) Paracchino, A.; Laporte, V.; Sivula, K.; Grätzel, M.; Thimsen, E. *Nat. Mater.* **2011**, *10*, 456−461.
(57) McDonald, K. J.; Choi, K. S. *Energy Environ. Sci.* **2012**, *5*, 8553−8557.
(58) Kay, A.; Cesar, I.; Grätzel, M. *J. Am. Chem. Soc.* **2006**, *128*, 15714−15721.